scientific reports

OPEN

Nonlinearly interacting entrainment due to shear and convection in the surface ocean

Yusuke Ushijima[1,2]✉ & Yutaka Yoshikawa[3]

Large-eddy simulations were performed to investigate the entrainment buoyancy flux at the mixed layer base due to nonlinearly interacting shear-driven turbulence (ST) and convective turbulence (CT). The fluxes due to pure ST and pure CT were first evaluated, and their scalings were derived. The entrainment flux due to coexisting ST and CT was then evaluated and compared to the scaling-based fluxes due to the pure turbulences. It was found that nonlinear effects reduce the entrainment flux by 30% when the turbulent kinetic energy production rates of ST and CT are comparable. The mixing parameterization schemes used in ocean general circulation models (OGCMs) fail to accurately reproduce the mixing due to the pure turbulences and/or the nonlinear effects, and thus the mixed layer depth (MLD). Because analysis using global datasets suggests that nonlinear effects are large at the mid-latitudes, these results indicate that the nonlinear effects might be responsible for the deep MLD biases in OGCMs and that mixing parameterization schemes need to be improved to correctly represent ocean surface mixing due to shear and convection, as well as waves, in OGCMs.

Vertical turbulent mixing induced by wind, surface cooling, and surface waves forms vertically uniform surface mixing/mixed layer (ML) in the upper stratified ocean. As the mixing deepens the ML, water below the ML is entrained into the layer, and ML water properties are changed. For example, the entrainment of colder and nutrient richer water changes temperature and the concentration of nutrients in the ML and then affects subsequent air-sea interaction[1,2] and primary production[3,4], respectively. It is in fact suggested that the ML deepening due to the entrainment enhances the variability of Pacific Decadal Oscillation and then affects the regional and global climate systems[2].

In ocean general circulation models (OGCMs), mixing parameterization schemes such as the Mellor–Yamada (MY) scheme[5] and the K-profile parameterization (KPP) scheme[6] are adopted to represent entrainment. Because the parameterization of the entrainment buoyancy flux at the ML base (P_b) is key to developing the mixing parameterization, the flux has been investigated in several studies[7–10]. Studies of the atmospheric boundary layer (ABL)[11–14] are also useful because the entrainment process in the ocean surface boundary layer is dynamically similar to that in the ABL. Many ABL studies[15,16] focused on the entrainment process caused by convective turbulence (CT) because it is likely dominant in the ABL.

In the ocean, CT is considered to be dominant if the sea surface is severely cooled. Deep convection down to 1000 m depth and greater in Labrador and Greenland seas is an example. When CT is dominant, temperature, salinity and momentum become almost uniform in the vertical. Under purely convective forcing (no wind forcing), the entrainment buoyancy flux at the ML base (P_b^C) in the ocean is considered to be proportional to the surface buoyancy flux (B_f, which is defined as positive for sea surface cooling) and is expressed as

$$P_b^C = -nB_f. \tag{1}$$

Here, $n \cong 0.2$[9,13,14] when convection is shallow. If, on the other hand, convection is deep and turnover time of convection L_{MLD}/W_* is longer than $1/f$, where $W_*[\equiv (B_f L_{MLD})^{1/3}]$ is convective velocity scale, L_{MLD} is ML depth (MLD), and f is the Coriolis parameter, the Earth rotation (the Coriolis acceleration term) acts and inhibits vertical velocity and hence CT[17]. Thus, the Earth's rotation decreases n at the convective Rossby number $Ro_b \equiv W_*/fL_{MLD} \lesssim 1$[18–20].

If, on the other hand, the sea surface is weakly cooled as in low-latitude ($< 10°$) regions, wind-induced shear-driven turbulence (ST) becomes dominant. When ST is dominant, temperature and salinity are well homogenized

[1]Japan Meteorological Business Support Center, Tsukuba 305-0052, Japan. [2]Meteorological Research Institute, Tsukuba 305-0052, Japan. [3]Graduate School of Science, Kyoto University, Kyoto 606-8502, Japan. ✉email: usijimay@mri-jma.go.jp

in the vertical while momentum is not, because the turbulent kinetic energy (TKE) in the ML is produced by the vertical shear of the horizontal velocity at each depth. At the ML base, the TKE is converted to the potential energy, and the entrainment buoyancy flux (P_b^S) is expressed as

$$P_b^S = -m\frac{U_*^3}{L_{MLD}},\tag{2}$$

where U_* is the friction velocity and m is a proportional coefficient[8]. It should be noted that the depth scale of the wind-induced shear is given by U_*/f (turbulent Ekman scale)[21] and the shear becomes almost zero at the depth below U_*/f in neutrally stratified fluid. This indicates that the shear at the ML base is weakened (intensified) if L_{MLD} is greater (smaller) than U_*/f. Consequently, m in Eq. (2) should depend on the Rossby number $Ro \equiv U_*/fL_{MLD}$[10,22]. However, the dependence of m on Ro has not been well investigated.

In autumn and winter, especially at mid-latitudes, ST and CT typically coexist in the ML. Some previous studies[9,10,23] assumed for simplicity that the entrainment buoyancy flux at the ML base due to coexisting ST and CT (P_b) can be expressed as the linear combination of the entrainment buoyancy fluxes due to pure ST and pure CT, that is,

$$P_b = P_b^S + P_b^C.\tag{3}$$

However, previous ABL studies showed that the ABL structure with coexisting ST and CT is different from the structure with each pure turbulence[24–26], and thus CT is suppressed in the entrainment zone (corresponding to the ML base in the ocean) by ST[14]. These results indicate that the effects of nonlinear interaction between ST and CT may also be large in the surface ocean, and thus the entrainment buoyancy flux P_b at the ML base cannot be expressed as a linear combination of P_b^S and P_b^C. Nevertheless, the nonlinear effects were not evaluated under realistic ocean surface forcing, and it is not clear when and where the nonlinear effects, if any, are large.

It is well known that recent OGCMs still have serious biases in simulating MLDs[27]. In recent decades, much attention has been directed to the shallow MLD biases in OGCMs and the effects of surface waves on these biases[27,28]. Surface waves interact with the wind-driven flow shear to form secondary circulations (Langmuir circulations) that induce turbulence and deepen the ML[29–31]. Non-breaking surface waves without wind-driven flow may also cause turbulence and deepen the ML[32,33]. Most OGCMs do not include these surface wave effects, and this is considered as one of the main reasons for the shallow MLD biases. Note, however, that deep MLD biases have also been found; the MLDs in OGCMs are sometimes greater than the observed values in regions such as the mid-latitudes (see Fig. 1 of Belcher et al.[28] and Fig. 11 of Tsujino et al.[34]), even though most OGCMs omit surface wave effects. This fact clearly demonstrates that entrainment processes due to ST and CT also need to be re-investigated quantitatively.

The aim of this study is to evaluate the entrainment buoyancy flux at the ML base induced by nonlinearly interacting ST and CT and quantify the nonlinear effects in the surface ocean. Surface wave effects are not considered here to isolate this interaction processes from other complicated processes. To this end, large-eddy simulations (LESs) of the upper-ocean turbulence forced by uniform steady wind stress and/or cooling were performed; the configuration is described in "Methods" section. Uniform and steady surface forcing is used as a first step to understand nonlinear interaction between ST and CT. In "Results" section, we first evaluated the parameter dependences of the entrainment buoyancy flux due to pure ST and pure CT and derived the scaling of each type of turbulence. Then, we quantified the nonlinear effects by comparing the entrainment flux due to coexisting ST and CT with the fluxes due to each pure turbulence under the realistic ocean forcing parameters. The mixing parameterization schemes used in OGCMs were also tested to see whether the entrainment buoyancy flux due to nonlinear effects as well as the pure turbulence is reproduced. The global distribution of the intensity of the nonlinearity is presented using global datasets in "Discussion" section.

Results

In this section, we first show simulated profiles of horizontally averaged flow, buoyancy, and TKE tendency terms in typical cases. Then, we evaluate the simulated entrainment buoyancy flux due to pure ST and pure CT to obtain their scalings (P_b^S and P_b^C, respectively). Using the scalings, we evaluate the simulated entrainment buoyancy flux due to coexisting ST and CT (P_b) and compare P_b with $P_b^S + P_b^C$ to quantify the nonlinear interaction effects between ST and CT. Finally, the mixing parameterization schemes are tested to evaluate the extent to which they reproduce the entrainment flux of the pure turbulences and the nonlinear effects.

Profiles of horizontally averaged velocity, buoyancy, and TKE tendency terms in the ML: Typical cases.
First, the results of typical cases of pure ST, pure CT, and coexisting ST and CT are shown. In this subsection, the initial stratification ($N_0 = 2.0 \times 10^{-2}$ s^{-1}), initial MLD ($L_0 = L_D/4$, where L_D is the domain size described in "Methods" section), and Coriolis parameter ($f = 10 \times 10^{-5}$ s^{-1}) are unchanged.

Figure 1 shows the temporal depth variation of the horizontally averaged current speed and buoyancy and vertical profiles of the TKE tendency terms [see Eq. (21) in "Methods" section] averaged over $4.0 < t/T_f < 5.0$, where t is time, and T_f ($= 2\pi/f$) is the inertial period. In the simulation of pure ST ($U_*^2 = 1.0 \times 10^{-4}$ m^2 s^{-2} and $B_f = 0$), the horizontal mean current speed oscillated with the inertial period (Fig. 1a). The entrainment of less buoyant water into the ML decreased the buoyancy in the ML, and the MLD (L_{MLD}) increased with time (Fig. 1d). Here, the MLD was defined as the depth at which the buoyancy production ($\mathcal{P}_b$), which is a TKE tendency term [Eq. (21)], was minimum[9]. Shear production ($\mathcal{P}_s$) was the dominant source of the pure ST, and the buoyancy production ($\mathcal{P}_b$) and dissipation ($\mathcal{D}_s$) were the sink terms in the ML (Fig. 1g). The convergence of the vertical transport of the TKE ($\mathcal{P}_t$) is positive in the lower ML, but it is much smaller than $\mathcal{P}_s$ in this case.
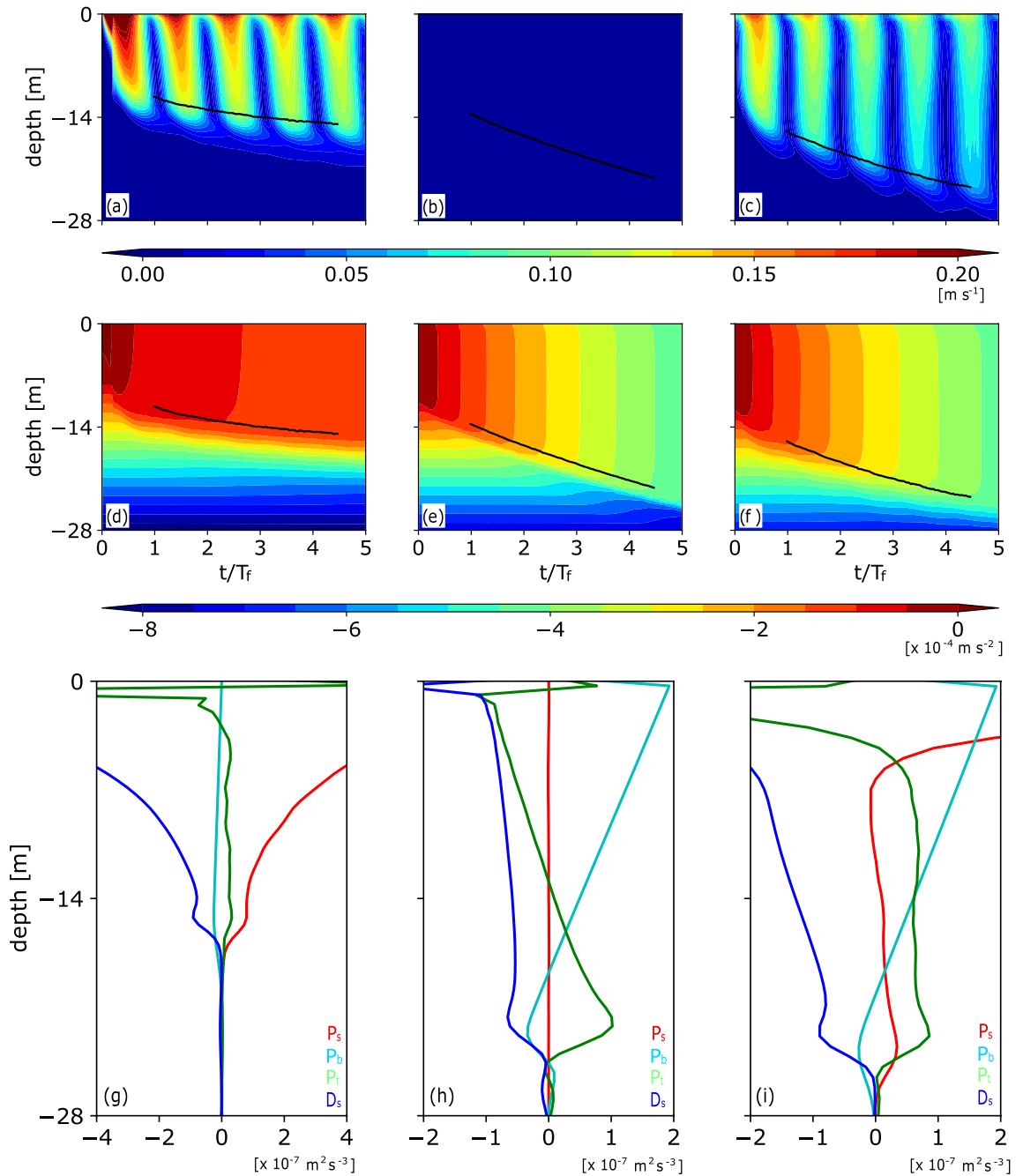
Figure 1. Time-depth variation of the horizontally averaged (a)–(c) current speed and (d)–(f) buoyancy (B) and (g)–(i) the vertical profiles of the TKE tendency terms averaged over $4.0 < t/T_f < 5.0$ in the (a), (d), (g) pure ST ($U_*^2 = 1.0 \times 10^{-4} \ \mathrm{m^2 \ s^{-2}}, B_f = 0$), (b), (e), (h) pure CT ($U_*^2 = 0, B_f = 19.6 \times 10^{-8} \ \mathrm{m^2 \ s^{-3}}$), and (c), (f), (i) coexisting ST and CT ($U_*^2 = 1.0 \times 10^{-4} \ \mathrm{m^2 \ s^{-2}}, B_f = 19.6 \times 10^{-8} \ \mathrm{m^2 \ s^{-3}}$) simulations. Initial stratification and initial MLD are $N_0 = 2.0 \times 10^{-2} \ \mathrm{s^{-1}}$ and $L_0 = L_D/4$, respectively. Solid lines in (a)–(f) represent the MLD.

In the simulation of pure CT ($U_*^2 = 0$ and $B_f = 19.6 \times 10^{-8} \ \mathrm{m^2 \ s^{-3}}$), the MLD increased with time, although the horizontal mean current speed was zero (Fig. 1b). The buoyancy in the ML decreased because of entrainment and surface buoyancy flux (Fig. 1e). Because there was no horizontal mean velocity shear, $\mathcal{P}_s$ was zero (Fig. 1h). $\mathcal{P}_b$ was positive in the upper ML, whereas it was negative in the lower ML. $\mathcal{P}_t$ was negative in the upper ML and positive in the lower ML, resulting in downward transport of the TKE in the ML.

In the simulation of coexisting ST and CT ($U_*^2 = 1.0 \times 10^{-4} \ \mathrm{m^2 \ s^{-2}}$ and $B_f = 19.6 \times 10^{-8} \ \mathrm{m^2 \ s^{-3}}$), the current became more vertically uniform in the ML than that in the pure ST simulation (Fig. 1a and c). $\mathcal{P}_s$ was positive in the ML, as in the pure ST simulation (Fig. 1g and i). In the lower ML, $\mathcal{P}_t$ was also positive, as in the pure CT simulation, and the contribution of $\mathcal{P}_t$ to the TKE tendency became larger at the MLD, in contrast to that in the pure ST simulation (Fig. 1g–i). The vertical profiles of $\mathcal{P}_s$ and $\mathcal{P}_t$ in this coexisting turbulence simulation differ
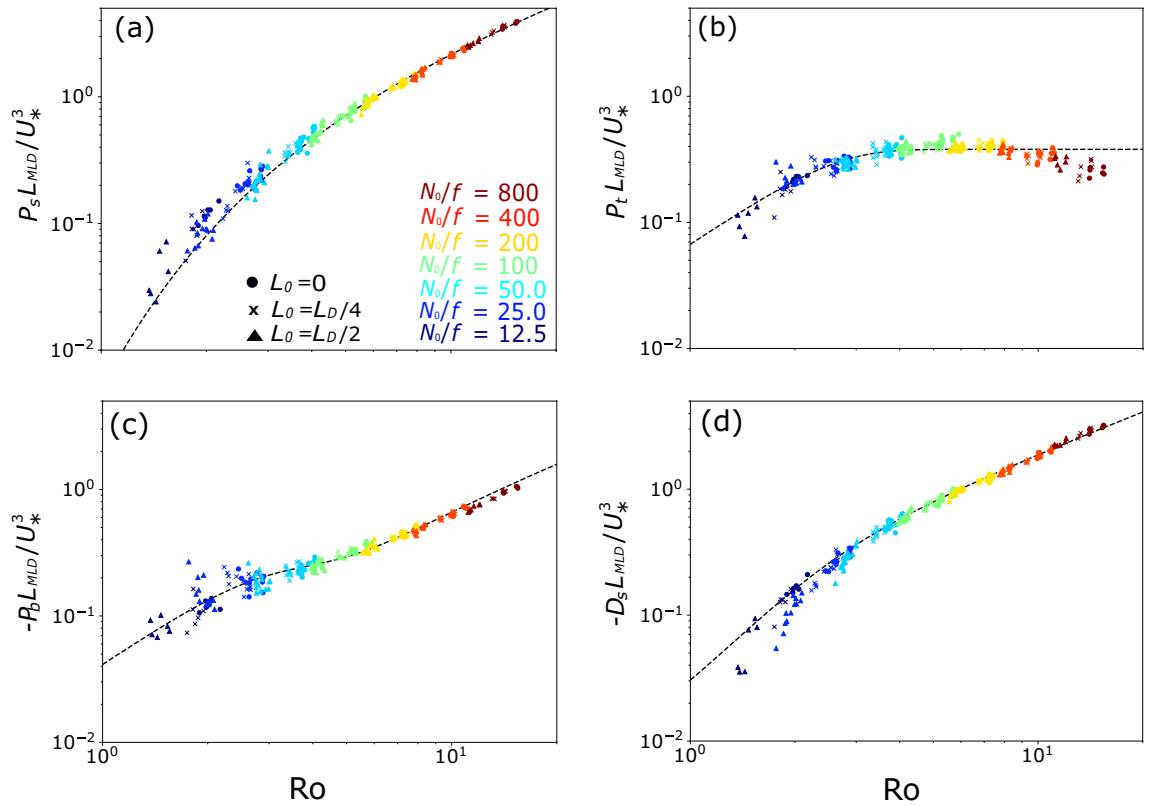
Figure 2. Scatter plots of Ro and (a) P_s, (b) P_t, (c)$-P_b$, and (d) $-D_s$ in the pure ST simulations ($B_f = 0$) averaged over $2.5 < t/T_f < 3.5$ and $4.0 < t/T_f < 5.0$. Each TKE tendency term was normalized by U_*^3/L_{MLD}. Symbols represent the initial MLD (L_0). Colors represent initial stratification (N_0/f). Dashed lines are the scalings derived in this study [Eqs. (4), (5), (7), and (8)].

from the linear combinations of those in the pure turbulence simulations, indicating that ST and CT interact nonlinearly with each other, as described in previous studies[24–26]. This result implies that the entrainment buoyancy flux (P_b), which corresponds to the buoyancy production rate ($\mathcal{P}_b$) at the MLD, due to coexisting ST and CT is also not represented by the linear combination of those fluxes induced by pure ST and pure CT.

TKE tendency terms at the ML base and their scalings for pure ST and pure CT. In this subsection, we evaluate the TKE tendency terms at the ML base for pure ST and pure CT to derive scalings of the entrainment buoyancy flux for these two pure cases (P_b^S and P_b^C, respectively). The scalings are used to quantify the nonlinear effects in coexisting ST and CT in the next subsection.

Pure ST case. The parameter dependence of the TKE tendency terms at the MLD in 135 pure ST simulations are reported here. Figure 2 shows a scatter plot of Ro ($\equiv U_*/fL_{MLD}$) and each TKE tendency term at the MLD (P_s, P_t, $-P_b$, and $-D_s$) normalized by U_*^3/L_{MLD} averaged over $2.5 < t/T_f < 3.5$ and $4.0 < t/T_f < 5.0$. Here, Ro and the TKE tendency terms at the MLD (P_s, P_t, $-P_b$, and $-D_s$) were sampled every $T_f/40$ and averaged for T_f. All these normalized tendencies decrease with decreasing Ro, except the normalized P_t at Ro greater than 3, where it is almost constant. These decreases are especially rapid at Ro < 3. Although P_t is much smaller than P_s in the typical case (where Ro ∼ 8) in the previous subsection, it become comparable at Ro ∼ 3 and larger at Ro ≲ 3.

The symbols and colors in Fig. 2 show the differences in initial MLD (L_0) and N_0/f, respectively. Note that despite the large number of simulations (135), the normalized tendency terms at the same Ro with different L_0 and N_0/f collapse onto a single line. Although previous studies[35,36] suggested that the TKE tendency terms without the Earth's rotation depend on Ri$_* \equiv \Delta B L_{MLD}/U_*^2 = N_0^2(L_{MLD}^2 - L_0^2)/2U_*^2$ (where ΔB is the vertical buoyancy difference across the MLD) and/or Fr $\equiv U_*/N_0 L_{MLD}$, we found that stratification had little effect on the TKE tendency terms in the present parameter range.

By least-square fitting, we obtained the scalings of P_s^S and P_t^S as

$$P_s^S = 0.33 \text{Ro} \exp\left(-\frac{4.2}{\text{Ro}}\right) \frac{U_*^3}{L_{MLD}}, \quad \text{and} \tag{4}$$
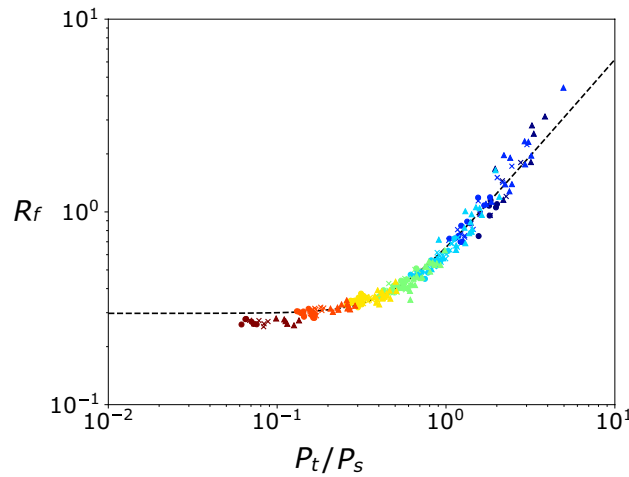
4

Figure 3. Scatter plot of P_t/P_s and the flux Richardson number $R_f (\equiv -P_b/P_s)$ in the pure ST simulations ($B_f = 0$) averaged over $2.5 < t/T_f < 3.5$ and $4.0 < t/T_f < 5.0$. Symbols and colors are the same as in Fig. 2. Dashed line is the regression line [Eq. (6)].

$$P_t^S = 0.38 \tanh\left(0.18\text{Ro}^{1.8}\right)\frac{U_*^3}{L_{MLD}}, \qquad (5)$$

where P_s^S and P_t^S are scaling-based tendencies for ST (while P_s, P_t, $-P_b$, and $-D_s$ are simulation-based tendency) and there functional forms were determined as described in "Methods" section. The scaling of P_b (i.e., P_b^S) was derived from the relationship between P_t/P_s and P_b/P_s. The flux Richardson number $R_f (\equiv -P_b/P_s)$ at the MLD seems to be constant if $P_s \gg P_t$[37,38], but it is expected to change as the rotation effect increases because P_s and P_t became comparable at Ro $\lesssim 3$ (Fig. 2a and b). From Fig. 3, the relationship between P_t/P_s and R_f was obtained as

$$R_f = \left[0.30^{\frac{5}{2}} + \left(0.62\frac{P_t}{P_s}\right)^{\frac{5}{2}}\right]^{\frac{2}{5}}; \qquad (6)$$

that is,

$$P_b^S = -\left[\left(0.30P_s^S\right)^{\frac{5}{2}} + \left(0.62P_t^S\right)^{\frac{5}{2}}\right]^{\frac{2}{5}}. \qquad (7)$$

Finally, the scaling of D_s (i.e., D_s^S) was obtained as

$$D_s^S = -(P_s^S + P_t^S + P_b^S), \qquad (8)$$

where we assumed almost steady TKE at the MLD (due to slow deepening of the ML). These relations reproduce well the simulated dependence of the TKE tendency terms on Ro (Fig. 2).

Pure CT case. For pure CT, the TKE tendencies are suggested to depend on B_f and $\text{Ro}_b \equiv W_*/fL_{MLD}$[18–20]. Figure 4 shows a scatter plot of Ro_b and each TKE tendency term (except P_s, because $P_s = 0$ in the pure CT cases) normalized by B_f in 50 pure CT simulations. At $\text{Ro}_b > 3$, all the normalized tendency terms are almost constant, and $P_b^C \cong -0.2B_f$, which is consistent with previous studies[9,19]. At $\text{Ro}_b < 3$, they decrease with decreasing Ro_b. Because the scaling of Wang[19] [$P_b^C = -0.2\tanh(\text{Ro}_b^{0.69})B_f$] slightly overestimated P_b at $\text{Ro}_b \sim 1$ (Fig. 4b), the scaling was modified in this study. By least-square fitting, we obtained

$$P_t^C = 0.48 \tanh\left(0.78\text{Ro}_b^{0.83}\right)B_f, \qquad (9)$$

$$P_b^C = -0.20 \tanh\left(0.78\text{Ro}_b^{0.83}\right)B_f, \quad \text{and} \qquad (10)$$

$$D_s^C = -0.23 \tanh\left(0.78\text{Ro}_b^{0.83}\right)B_f, \qquad (11)$$

where P_t^C, P_b^C, and D_s^C are scaling-based tendencies for CT. Here, $P_t^C + P_b^C + D_s^C \neq 0$ because the temporal change in the TKE is large (i.e., ongoing ML deepening occurs), in contrast to that in the pure ST cases.

Nonlinear effects of ST and CT interaction at the ML base. Using the scalings of the TKE tendency terms for pure ST (P_s^S [Eq. (4)], P_t^S [Eq. (5)], and P_b^S [Eq. (7)]) and pure CT (P_t^C [Eq. (9)] and P_b^C [Eq. (10)]) and
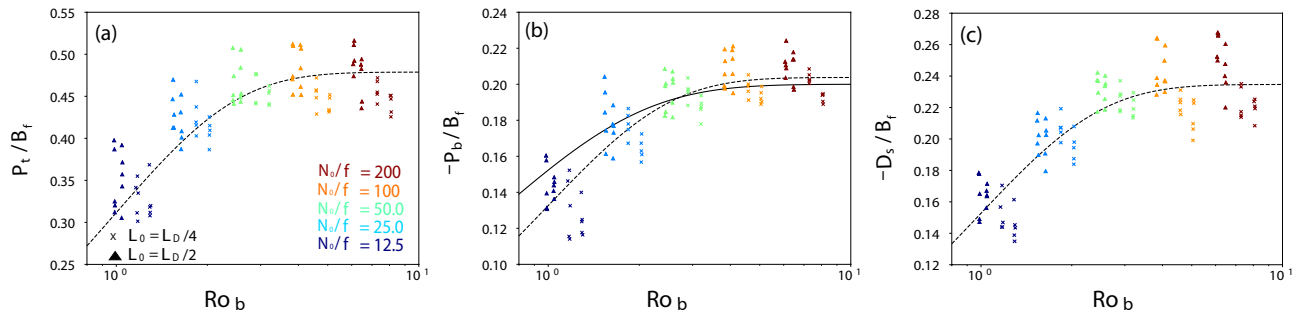
Figure 4. Scatter plots of Ro_b and (a) P_t, (b) $-P_b$, and (c) $-D_s$ in the pure CT simulations ($U_*^2 = 0$) averaged over $2.5 < t/T_f < 3.5$ and $4.0 < t/T_f < 5.0$. Each TKE tendency term was normalized by B_f. Symbols and colors are the same as in Fig. 2. Dashed lines are the scalings derived in this study [Eqs. (9)–(11)], and solid line in (b) is the scaling of[19] [$0.2 \tanh(Ro_b^{0.69})$].

simulation-based tendency of P_s, P_t and P_b for 450 simulatinos of coexisting ST and CT, the nonlinear effects of ST and CT interaction at the MLD are evaluated. Figure 5a shows P_s/P_s^S (ratio of the simulated shear production with CT to the scaling-based shear production due to pure ST) as a function of P_b^C/P_b^S (a measure of CT relative to ST). Note that P_s/P_s^S was excluded if $P_t/P_s > 100$ because P_s has little effect on TKE tendency. P_s/P_s^S increases with P_b^C/P_b^S, indicating that ST is intensified by CT. For example, P_s becomes 20–30 times larger than P_s^S at $P_b^C/P_b^S \cong 10^2$. Note, however, that as CT becomes more dominant, P_t has more impact on the TKE tendency than P_s [see the color representing the intensity of P_t relative to P_s (P_t/P_s) in Fig. 5a]. Figure 5b shows $-(P_s - P_s^S)/P_b$, a ratio of the increased shear production by CT ($P_s - P_s^S$) to the entrainment buoyancy flux (P_b), as a function of P_b^C/P_b^S. The impact of the increased shear by CT on the entrainment is found largest at around $P_b^C/P_b^S = 10^{1/2}$.

Previous studies[14,39], on the other hand, suggested that CT is inhibited by ST. To see this effect, we plot $P_t/(P_t^S + P_t^C)$ as a function of P_b^C/P_b^S in Fig. 5c. Here, P_t is a measure of CT at the MLD, and the ratio of P_t to $P_t^S + P_t^C$ represents the intensity of the nonlinear interaction effects. P_t was 40 % smaller than $P_t^S + P_t^C$ at $10^{-1/2} < P_b^C/P_b^S < 10^{1/2}$, indicating that ST and CT interact nonlinearly to decrease P_t in this parameter range. This indicates that ST disrupts coherent structure of pressure and/or TKE and vertical velocity [see Eq. (21) in "Methods" section] associated with convective motion (CT). This P_t decrease [$P_t - (P_t^S + P_t^C)$] by the interaction contributes more to P_b than the increased P_s by the interaction (Fig. 5b and d). Consequently, P_b became 30 % smaller than $P_b^S + P_b^C$ at $1 < P_b^C/P_b^S < 10^{3/2}$ (Fig. 5e).

Entrainment flux in the ocean mixing parameterization schemes used in OGCMs. In the previous subsection, we suggested that the nonlinear interaction between ST and CT likely inhibits the entrainment at the ML base at $1 < P_b^C/P_b^S < 10^{3/2}$. To accurately simulate the ML-related processes using OGCMs, the mixing parameterization schemes should reproduce the entrainment buoyancy flux of the nonlinear interaction effects as well as those of the pure turbulences. To see the extent to which the schemes reproduce the entrainment flux of the pure turbulences and the nonlinear effects, one-dimensional (1D) simulations with the mixing parameterization schemes were performed, and the results are compared to the LES results in this subsection.

The mixing parameterization schemes tested in this study were the KPP scheme[6], level 2.5 MY scheme[5,40,41], and level 2.5 Nakanishi–Niino (NN) scheme[42–44]. The NN scheme is a modified version of the MY scheme and is used in ocean models[45] as well as atmospheric models[46,47]. The boundary and initial conditions were the same as those in the LES. The detail configuration for 1D simulations is described in "Methods" section.

Figure 6 shows scatter plots of Ro ($\equiv U_*/fL_{MLD}$) and P_b^S normalized by U_*^3/L_{MLD} for the 1D pure ST simulations (cf. Fig. 2c), Ro_b ($\equiv W_*/fL_{MLD}$) and P_b^C normalized by B_f for the 1D pure CT simulations (cf. Fig. 4c), and P_b^C/P_b^S and P_b normalized by $P_b^S + P_b^C$ in the 1D simulations of coexisting ST and CT (cf. Fig. 5c). Figure 6 also shows the temporal change in MLD in the 1D simulations using the typical parameters used in the LESs shown in Fig. 1. For pure ST, the normalized P_b^Ss in the KPP and MY schemes show more scattering than those in the LES at Ro > 3, suggesting that these schemes are likely affected by other factors such as Ri_* and/or Fr, which had little effect on P_b^S in the LESs in the present parameter range (Fig. 6a). Because these normalized P_b^Ss were also underestimated, the ML deepened less from $t/T_f = 1$ to $t/T_f = 4.5$ than it did in the LES (Fig. 6d). The NN scheme successfully reproduced the dependence of P_b^S on Ro with less scatter, but it overestimated P_b^S (Fig. 6a) and thus the MLD (Fig. 6d).

The scalings of P_b^S in these schemes were evaluated for later use. For simplicity, P_b^S was assumed to be proportional to Ro^d, where d is constant. By least-square fitting, we obtained

$$P_b^{S-KPP} = -0.090 Ro^{0.43} \frac{U_*^3}{L_{MLD}}, \tag{12}$$

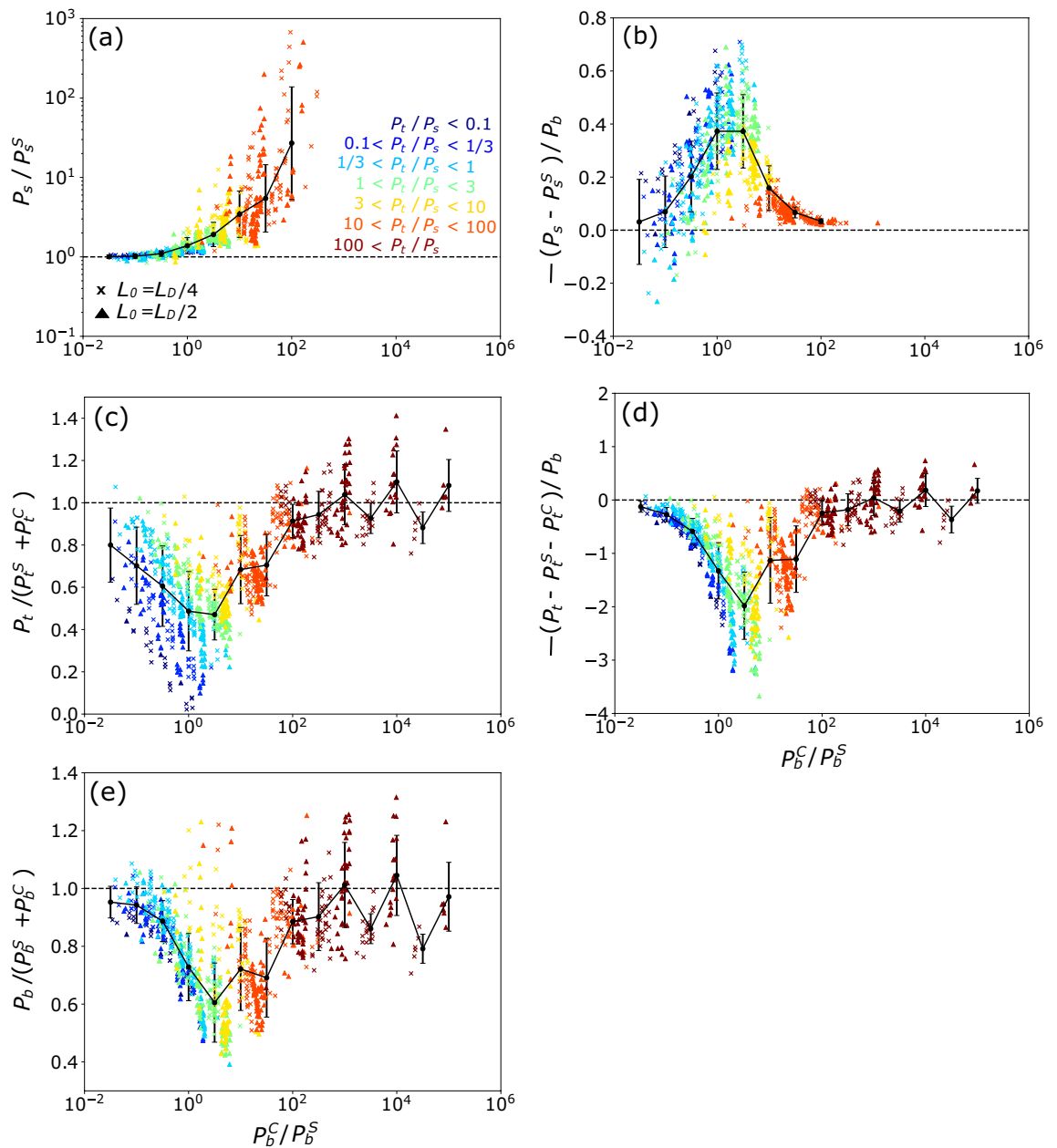$$P_b^{S-MY} = -0.0052 Ro^{1.4} \frac{U_*^3}{L_{MLD}}, \quad \text{and} \tag{13}$$

6

Figure 5. Scatter plots of (a) P_b^C/P_b^S and P_s/P_s^S, (b) P_b^C/P_b^S and $(P_s - P_s^S)/P_b$, (c) P_b^C/P_b^S and $P_t/(P_t^S + P_t^C)$, (d) P_b^C/P_b^S and $[P_t - (P_t^S + P_t^W)]/P_b$, and (e) P_b^C/P_b^S and $P_b/(P_b^S + P_b^C)$ in the coexisting ST and CT simulations. Symbols are the same as in Fig. 2. Colors represent P_t/P_s. Black circle and bar show the averaged value and standard deviation, respectively.

$$P_b^{S-NN} = -0.11\text{Ro}^{0.94}\frac{U_*^3}{L_{MLD}}. \tag{14}$$

For pure CT, on the other hand, the normalized P_b^Cs in the KPP and NN schemes were similar to those of the LES, whereas those in the MY scheme were much smaller (Fig. 6b). As a result, the MLDs were well reproduced by the KPP and NN schemes and underestimated by the MY scheme (Fig. 6e). The decreases in P_b^C with decreasing Ro_b were smaller in all of these schemes than in the LES (Fig. 6b), probably because they do not include the effects of Earth's rotation. Here, we assume $P_b^C \propto B_f$ and derive the scalings of P_b^C in these schemes by least-square fitting as

$$P_b^{C-KPP} = -0.16B_f, \tag{15}$$

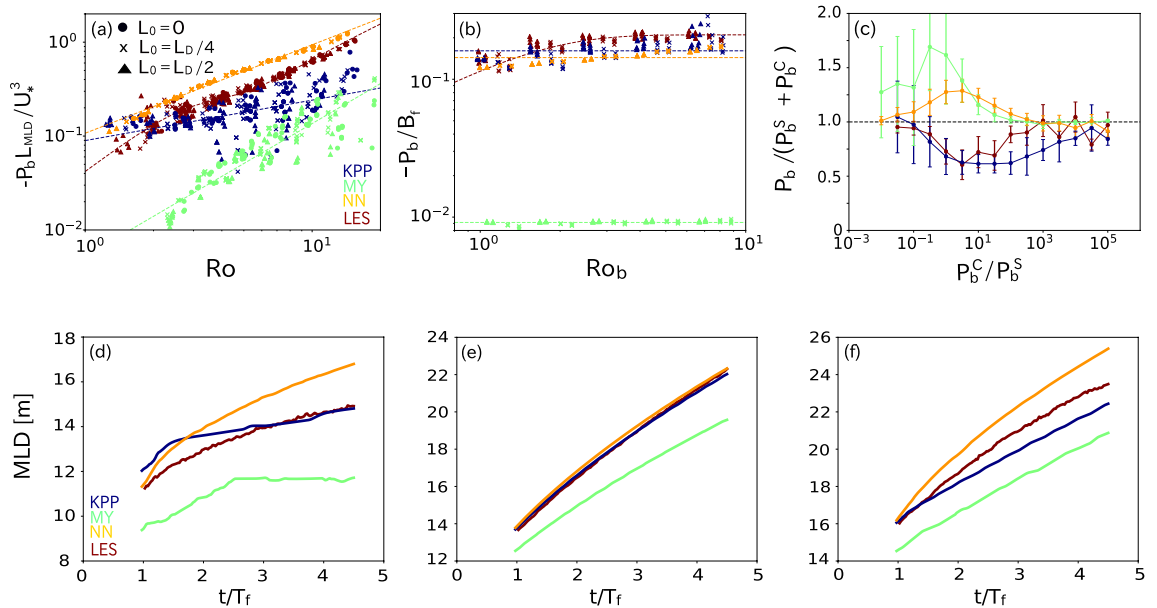$$P_b^{C-MY} = -0.0091B_f, \quad \text{and} \tag{16}$$

Figure 6. Same as (a) Fig. 2c, (b) Fig. 4b, and (c) Fig. 5e but for the results of the LES (red) and 1D simulations with the KPP (blue), MY (green), and NN (orange) schemes. Temporal variation of the MLD in the simulations with the typical parameters of (d) pure ST, (e) pure CT, and (f) coexisting ST and CT. The parameters used in (d)–(f) are the same as those in Fig. 1a–c, respectively. Time is normalized by T_f. Colors represent the LES (red) and the KPP (blue), MY (green), and NN (orange) schemes.

$$P_b^{C-NN} = -0.14 B_f. \tag{17}$$

The nonlinear interaction effects between ST and CT in these mixing parameterization schemes were quantified using these scalings [Eqs. (12)–(17)] (Fig. 6c). The P_bs in the MY and NN schemes are greater than $P_b^S + P_b^C$, indicating that they tend to represent the interaction effects in an opposite sense. The MLD was underestimated by the MY scheme (Fig. 6f) owing to the underestimations of P_b^S (Fig. 6a) and P_b^C (Fig. 6b), despite the failure to reproduce the nonlinear effects (Fig. 6c). On the other hand, the MLD was overestimated by the NN scheme (Fig. 6f) because of the overestimation of P_b^S (Fig. 6a) and the failure to reproduce the nonlinear effects (Fig. 6c). The KPP scheme successfully reproduced the nonlinear effects except at $P_b^C/P_b^S > 10$ (Fig. 6c), although the underestimation of P_b^S resulted in the underestimation of the MLD (Fig. 6f). Note that the above differences between the LES and mixing schemes would become smaller by tuning empirical parameters in the schemes, though it seems uneasy to reduce the differences in the pure and coexisting turbulence regimes simultaneously.

Discussion

In this section, we estimate the global distribution of the intensity of the nonlinear effects in the real ocean. The parameters Ro, W_*^3/U_*^3, and Ro$_b$ were calculated from the U_*, B_f, and L_{MLD} in observed and reanalysis data in autumn and winter (see "Methods" section) and are shown in Fig. 7. (Note that the U_*^3/L_{MLD}-normalized P_b^S and P_b^C depend only on these parameters.) Here, data at $B_f < 0$ were excluded from the analysis. (These data were often found near the equator.) Figures 7a and b show that Ro is larger due to smaller f and amounts to $10^{1/2}(= 3.2)$ or more in tropical regions ($< 20°$). On the other hand, W_*^3/U_*^3 is small ($< 10^{1/2}$) at lower latitude than $15°$ and higher latitude than $40°$ and large ($> 10^{1/2}$) at mid-latitude ($15°$–$40°$) (Fig. 7c and d). As a result, ST is more dominant than CT ($P_b^C/P_b^S < 1$) at the low and high latitudes (Fig. 7g and h). At higher latitude than $45°$ N in the North Atlantic, W_*^3/U_*^3 is also large (Fig. 7c and d), and hence $P_b^C/P_b^W > 10^{3/2}$ (Fig. 7g and h), especially in winter. However, Ro$_b < 1$ in winter (Fig. 7e and f) suggests that deep water formation in the North Atlantic is inhibited by Earth's rotation[17]. Note that at mid-latitudes, P_b^C/P_b^S ranges from 1 to $10^{3/2}$, indicating that the nonlinear interaction between ST and CT is expected.

To estimate geological distribution of the expected nonlinear interaction intensity (Fig. 7i and j), we used Fig. 8, where scatter plots of Ro and W_*^3/U_*^3 from the observed (Fig. 8a) and simulated (Fig. 8b) data are shown. In Fig. 8b, the intensity of the nonlinear effects [$P_b/(P_b^S + P_b^C)$] averaged over bins on (Ro, W_*^3/U_*^3) space is also shown. Here, the observed (Ro, W_*^3/U_*^3) at a certain grid point (Fig. 7a-d and 8a) was converted to $P_b/(P_b^S + P_b^C)$ using simulated relation between (Ro, W_*^3/U_*^3) and bin-averaged $P_b/(P_b^S + P_b^C)$ in Fig. 8b, and this was considered as observed $P_b/(P_b^S + P_b^C)$. The cross-hatching in Fig. 7i and j represents the region where Ro and W_*^3/U_*^3 are outside of the simulated parameter range. These figures show that our simulations covered most of the observed pairs of Ro and W_*^3/U_*^3, except in the Southern Ocean, where surface cooling is weak relative to wind stress ($W_*^3/U_*^3 < 0.1$) and ST is expected to strongly dominate CT. The observed $P_b/(P_b^S + P_b^C)$ is less than 0.8 at mid-latitudes and 0.6 at some region between $15°$ and $25°$, indicating that the nonlinear interaction between ST and CT probably suppresses the entrainment at the ML base there. Because some mixing parameterization schemes such as the MY and NN schemes cannot reproduce the nonlinear effects, the fact that the schemes did
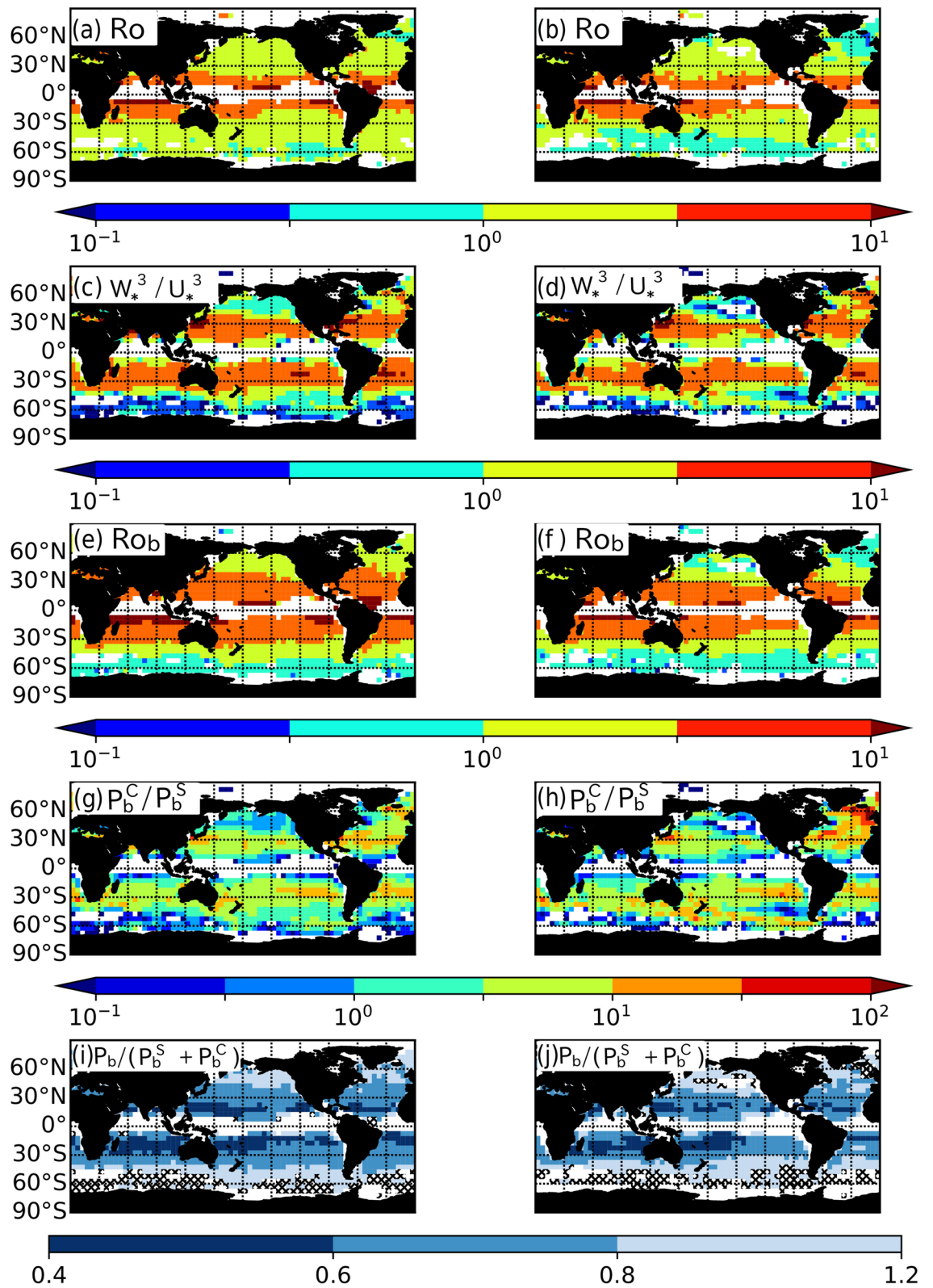
Figure 7. Seasonal (three month) averages of (a), (b) $\mathrm{Ro}(\equiv U_*/fL_{MLD})$, (c), (d) W_*^3/U_*^3, (e), (f) $\mathrm{Ro}_b(\equiv W_*/fL_{MLD})$, (g), (h) P_b^C/P_b^S, and (i), (j) $P_b/(P_b^S + P_b^C)$ in (a), (c), (e), (g), (i) autumn and (b), (d), (f), (h), (j) winter estimated from observations in 2001–2010. $P_b/(P_b^S + P_b^C)$ in (i) and (j) were evaluated from the observed (Ro, W_*^3/U_*^3) and the simulated bin-averaged relationship between (Ro, W_*^3/U_*^3), and $P_b/(P_b^S + P_b^C)$ shown in Fig. 8b.
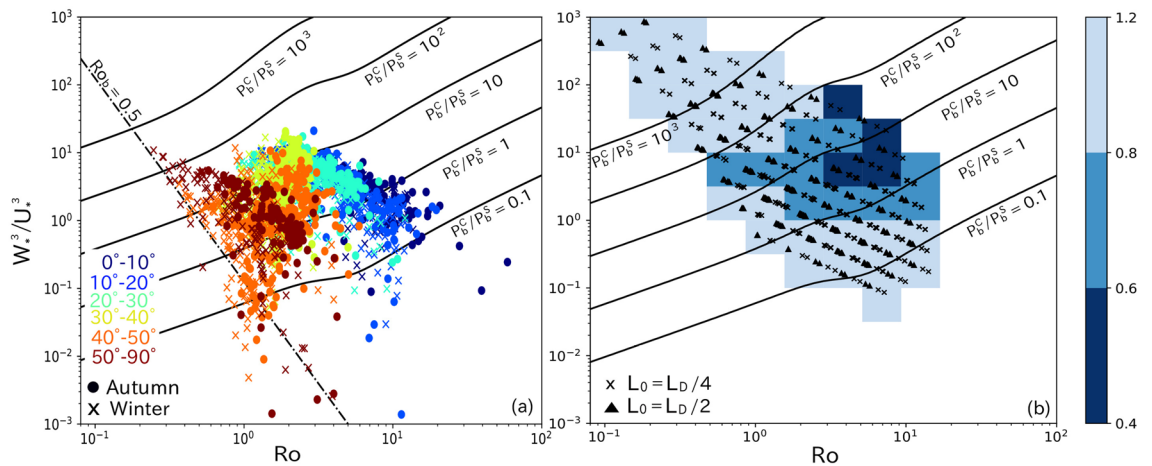
Figure 8. Scatter plots of Ro and W_*^3/U_*^3 calculated from (a) observed data and (b) LES data. Symbols in (a) and (b) represent seasons and initial MLD (L_0), respectively. Color represents latitude in (a) and bin-averaged $P_b/(P_b^S + P_b^C)$ in (b). Solid lines are contour lines of P_b^C/P_b^S, and dash-dotted line in (a) is contour line of $Ro_b = 0.5$.

not successfully reproduce the effect of nonlinear interaction between ST and CT might explain the mid-latitude deep MLD biases in winter observed in some OGCMs as seen in Fig. 1 of Belcher et al.[28] and Fig. 11 of Tsujino et al.[34]. [More than half OGCMs in the Coupled Model Intercomparison Project phase 6 evaluated by Tsujino et al.[34] adopted schemes similar to the MY and NN schemes (1.5 or higher order turbulence closure schemes), though each of the schemes used slightly different parameterizations and/or tuning parameters from those of the MY and NN schemes.] This result suggests that mixing parameterization schemes need to be checked and improved (if necessary) to correctly represent ocean surface mixing due to ST and CT.

In this study, we found the nonlinear interaction between ST and CT is expected large in mid-latitude ML in the ocean. However, the interaction mechanism remains to be investigated in more detail. We also found that the KPP, MY, and NN schemes do not well represent pure ST mixing. Because ST likely plays more role in the ocean than in the atmosphere, we consider that this issue should not be overlooked in ML mixing schemes. Effects of wave and/or time-varying forcing as well as heterogeneous background environment (such as ocean front) also need to be considered simultaneously for realistic ML simulation in the OGCMs. These will be studied in future.

Methods

Simulations and data. *Numerical model and experimental configurations for large-eddy simulations.* The LES model used in this study is the same as that used in Ushijima and Yoshikawa[48,49]. The governing equations are the momentum equation, continuity equation, and advection–diffusion equation of buoyancy under the incompressible, *f*-plane, Boussinesq, and rigid-lid approximations. Subgrid-scale parameterization follows the method described by Deardorff[50] and Maronga et al.[51]. At the surface, constant wind stress ($\rho_0 U_*^2$, where $\rho_0 = 1.0 \times 10^3$ kg m^{-3} is the reference water density) and buoyancy flux (B_f) were imposed. We also imposed subgrid-scale shear production at the surface. At the bottom, the free-slip condition and no-buoyancy flux condition were imposed. The lateral boundaries were periodic in both directions. The initial stratification ($N \equiv \sqrt{\partial B/\partial z}$, where B is the horizontally averaged buoyancy) was zero ($N = 0$) from the surface ($z = 0$) to the initial MLD ($z = -L_0$) and constant ($N = N_0$) from $z = -L_0$ to the bottom of the ocean ($z = -L_D$, where L_D is the domain length).

To evaluate the buoyancy entrainment flux due to pure ST, pure CT, and coexisting ST and CT, simulations were performed with several values of the momentum flux (U_*^2), surface buoyancy flux (B_f), initial stratification ($N_0 = 0.125, 0.25, 0.5, 1.0$, and 2.0×10^{-2} s^{-1}, corresponding to temperature changes of 0.078, 0.31, 1.3, 5, and 20 K in 100 m), initial MLD (L_0), and Coriolis parameter (f). In the simulations of pure ST, we set $U_*^2 = 0.5, 1.0$, and 2.0×10^{-4} m^2 s^{-1} (corresponding to wind speeds at 10 m height of 7, 10, and 14 m s^{-1}), $B_f = 0, L_0 = 0, L_D/4$, and $L_D/2$, and $f = 2.5, 5.0$, and 10×10^{-5} s^{-1} (corresponding to latitudes of 10°, 20°, and 40° N). In the simulations of pure CT, we set $U_*^2 = 0$, $B_f = 1.225, 2.45, 4.9, 9.8$, and 19.6×10^{-8} m^2 s^{-3} (corresponding to surface cooling of 25, 50, 100, 200, and 400 W m^{-2}), $L_0 = L_D/4$ and $L_D/2$, and $f = 10 \times 10^{-5}$ s^{-1}. A total of 135 and 50 simulations were performed for pure ST and pure CT, respectively. To examine the nonlinear interaction between ST and CT, a total of 450 simulations with $U_*^2 = 0.5, 1.0$, and 2.0×10^{-4} m^2 s^{-2}, $B_f = 1.225, 2.45, 4.9, 9.8$, and 19.6×10^{-8} m^2 s^{-3}, $L_0 = L_D/4$ and $L_D/2$, and $f = 2.5, 5.0$, and 10×10^{-5} s^{-1} were performed. These parameters are determined from the typical values of the observed climatologies in autumn and winter.

The governing equations were discretized using the second-order finite-difference scheme and integrated in time using the second-order Runge–Kutta scheme. The number of grid cells was $64 \times 64 \times 64$, and the grid spacing was uniform. The domain size, $L_D \times L_D \times L_D$, was varied according to the friction velocity (U_*), buoyancy flux (B_f), initial stratification (N_0), and Coriolis parameter (f). In the simulations of pure ST and coexisting

ST and CT, L_D was set to $4L_{P73}(1 + 5.1B_f/U_*^2N_0)$, where $L_{P73} \equiv U_*/\sqrt{N_0 f}$ is the MLD scale characterizing the wind-induced ML in the stratified ocean under the Earth's rotation[49,52], whereas L_D was set to $17\sqrt{B_f/N^2 f}$ in the simulations of pure CT. We performed several LESs with quarter-grid spacing but the same domain size and found that the TKE tendency terms obtained in the simulations with higher resolution were almost the same as those obtained with the original resolution. The dependence on the resolution is discussed in detail in Supplementary Information. The integration was continued for $5T_f$, where $T_f = 2\pi/f$ is the inertial period.

Experimental configurations for one-dimensional simulations with mixing parameterization schemes. The governing equations for one-dimensional (1D) simulations are momentum equation and diffusive equation of buoyancy,

$$\frac{\partial U}{\partial t} - fV = \frac{\partial}{\partial z}\left(K_M \frac{\partial U}{\partial z}\right),$$ (18)

$$\frac{\partial V}{\partial t} + fU = \frac{\partial}{\partial z}\left(K_M \frac{\partial V}{\partial z}\right), \quad \text{and}$$ (19)

$$\frac{\partial B}{\partial t} = \frac{\partial}{\partial z}\left(K_S \frac{\partial U}{\partial z}\right),$$ (20)

where (U, V) is the horizontal velocity components, B is buoyancy, and K_M and K_S are the eddy viscosity and diffusivity, determined in the KPP[6], MY[5,40,41], or NN[42–44] schemes, respectively. The boundary condition at the surface and the bottom, domain depth (L_D), and the number of the vertical grid cells, are same as those in the LES. A total of 135, 50, and 450 simulations for pure ST, pure CT, and coexisting ST and CT were respectively performed for each 1D experiment with different mixing schemes with same momentum flux (U_*), buoyancy flux (B_f), initial stratification (N_0), initial MLD (L_0), and Colioris parameter as those in the LES.

Observed and reanalysis data. Data were analyzed for autumn (October, November, and December in the northern hemisphere and April, May, and June in the southern hemisphere) and winter (January, February, and March in the northern hemisphere and July, August, and September in the southern hemisphere), when ST and CT are typically expected to coexist. The climatology of the ML temperature (T_{ML}) and salinity (S_{ML}) as well as the MLD (L_{MLD}) of the mixed layer Argo dataset, gridpoint value (MILA-GPV)[53] were used. The surface fluxes were the 6-hourly momentum fluxes (τ_x, τ_y), net heat flux (H_f), and freshwater flux ($E - P$) from the National Centers for Environmental Prediction (NCEP) data[54] for 2001–2010, where E and P are the evaporation rate and precipitation rate, respectively. The shortwave radiation was assumed not to penetrate below the surface for simplicity, and the evaporation rate was estimated from the latent heat flux with the latent heat vaporization of water[55]. These fluxes were converted to the friction velocity $U_*[= (\tau_x^2 + \tau_y^2)^{1/4}/\rho_0^{1/2}]$ and buoyancy flux $B_f[= -\alpha g H_f/\rho_0 C_a + \beta g(E - P)S_{ML}]$. Here, $\rho_0 (= 1.0 \times 10^3 \text{ kg m}^{-3})$ and $C_a (= 4.0 \times 10^3 \text{ J kg}^{-1} \text{ C}^{-1})$ are the reference density and heat capacity of water, respectively. The thermal expansion rate (α) and haline contraction rate (β) were calculated from T_{ML} and S_{ML} using the equation of state for seawater[56]. The momentum flux, buoyancy flux, and MLD were averaged into seasonal (three-month) climatological data points. The horizontal resolution of the data was $5° \times 5°$.

Analysis. *TKE tendency terms in the LES.* The TKE tendency terms were calculated as

$$\frac{\partial}{\partial t}\left(\frac{1}{2}\overline{u'_k u'_k} + \overline{e}\right) = \underbrace{-(\overline{u'_k w'} - 2\overline{v s_{k3}})\frac{\partial \overline{u_k}}{\partial z}}_{\mathcal{P}_s} + \underbrace{\overline{w'b'} - \kappa\frac{\overline{\partial b}}{\partial z}}_{\mathcal{P}_b} - \underbrace{\frac{\partial}{\partial z}\left(\frac{1}{2}\overline{u'_k u'_k w'} + \frac{\overline{\pi' w'}}{\rho_0} + \overline{w'e} + 2\overline{u'_k v s_{k3}} + 2v\frac{\overline{\partial e}}{\partial z}\right)}_{\mathcal{P}_t} \underbrace{-\overline{\varepsilon}}_{\mathcal{D}_s},$$ (21)

where u_i represents the velocity components (u, v, w) in the x_i direction, $x_i(i = 1, 2, 3)$ denotes the Cartesian coordinates (x, y, z), b is buoyancy, $\pi = p + 2\rho_0 e/3$ is modified pressure, p is pressure, and $s_{ij} \equiv (\partial u_i/\partial x_j + \partial u_j/\partial x_i)/2$. The subgrid-scale kinetic energy (e), eddy viscosity (v), eddy diffusivity (κ), and dissipation rate (ε) were calculated using sub-grid scale parameterization[50,51]. The overbar represents the horizontal average, and the prime indicates anomalies from the horizontal average. In the above equation, $\mathcal{P}_s$, $\mathcal{P}_b$, $\mathcal{P}_t$, and $\mathcal{D}_s$ represent the rates of shear production, buoyancy production, convergence of vertical transport of the TKE, and dissipation of the TKE, respectively. (Note that they are a function of z.)

Functional forms of the P_s^S and P_t^S scalings. In the pure ST simulations, the normalized P_s is almost linearly proportional to Ro at large Ro, but the slope increases for smaller Ro (Fig. 2a). Under neutral stratification, the vertical shear of the horizontal velocity (the Ekman velocity shear) decreases with depth ($|z|$) as $\exp(-|z|/L_{EKD})$, where $L_{EKD} \equiv U_*/f$ is the depth of the turbulent Ekman layer[21]. Therefore, the vertical shear at the MLD is expected to be proportional to $\exp[-cL_{MLD}/(U_*/f)] = \exp(-c/\text{Ro})$, where c is a constant. Consequently, we assume that the normalized P_s is proportional to $\text{Ro} \exp(c/\text{Ro})$.

On the other hand, the normalized P_t at Ro < 3 decreases with decreasing Ro but does not vary significantly with Ro at Ro > 3 (Fig. 2b). Because the variation of this normalized P_t^S with Ro is similar to that of the

normalized P_t^C with Ro_b in the pure CT simulations, we assume that the normalized P_t^S has the same functional form as the normalized P_t^C [Eq. (9)].

Data availability

References

1. Kataoka, T., Kimoto, M., Watanabe, M. & Tatebe, H. Wind-mixed layer-SST feedbacks in a tropical air–sea coupled system: Application to the Atlantic. *J. Clim.* **32**, 3865–3881. https://doi.org/10.1175/JCLI-D-18-0728.1 (2019).
2. Newman, M. *et al.* The pacific decadal oscillation, revisited. *J. Clim.* **29**, 4399–4427. https://doi.org/10.1175/JCLI-D-15-0508.1 (2016).
3. Obata, A., Ishizaka, J. & Endoh, M. Global verification of critical depth theory for phytoplankton bloom with climatological in situ temperature and satellite ocean color data. *J. Geophys. Res.* **101**, 20657–20667. https://doi.org/10.1029/96JC01734 (1996).
4. Martinez, E., Antoine, D., d'Ortenzio, F. & de Boyer Montégut, C. Phytoplankton spring and fall blooms in the north Atlantic in the 1980s and 2000s. *J. Geophys. Res. Oceans* **116**, https://doi.org/10.1029/2010JC006836 (2011).
5. Mellor, G. L. & Yamada, T. Development of a turbulence closure model for geophysical fluid problems. *Rev. Geophys.* **20**, 851–875. https://doi.org/10.1029/RG020i004p00851 (1982).
6. Large, W. G., Mcwilliams, J. C. & Doney, S. C. Oceanic vertical mixing: A review and a model with a nonlocal boundary-layer parameterization. *Rev. Geophys.* **32**, 363–403. https://doi.org/10.1029/94rg01872 (1994).
7. Turner, J. & Kraus, E. A one-dimensional model of the seasonal thermocline I. A laboratory experiment and its interpretation. *Tellus* **19**, 88–97. https://doi.org/10.1111/j.2153-3490.1967.tb01461.x (1967).
8. Kraus, E. & Turner, J. A one-dimensional model of the seasonal thermocline II. The general theory and its consequences. *Tellus* **19**, 98–106. https://doi.org/10.3402/tellusa.v19i1.9753 (1967).
9. Noh, Y., Goh, G. & Raasch, S. Examination of the mixed layer deepening process during convection using les. *J. Phys. Oceanogr.* **40**, 2189–2195. https://doi.org/10.1175/2010JPO4277.1 (2010).
10. Zhu, Y. & Zhang, R.-H. Scaling wind stirring effects in an oceanic bulk mixed layer model with application to an OGCM of the tropical pacific. *Clim. Dyn.* **51**, 1927–1946. https://doi.org/10.1007/s00382-017-3990-5 (2018).
11. Tennekes, H. & Driedonks, A. Basic entrainment equations for the atmospheric boundary layer. *Bound. Layer Meteor.* **20**, 515–531. https://doi.org/10.1007/BF00122299 (1981).
12. Driedonks, A. Models and observations of the growth of the atmospheric boundary layer. *Bound. Layer Meteor.* **23**, 283–306. https://doi.org/10.1007/BF00121117 (1982).
13. Pino, D., Vilà-Guerau de Arellano, J. & Duynkerke, P. G. The contribution of shear to the evolution of a convective boundary layer. *J. Atmos. Sci.* **60**, 1913–1926, https://doi.org/10.1175/1520-0469(2003)060<1913:TCOSTT>2.0.CO;2 (2003).
14. Pino, D. & De Arellano, J.V.-G. Effects of shear in the convective boundary layer: Analysis of the turbulent kinetic energy budget. *Acta Geophys.* **56**, 167–193. https://doi.org/10.2478/s11600-007-0037-z (2008).
15. Tennekes, H. A model for the dynamics of the inversion above a convective boundary layer. *J. Atmos. Sci.* **30**, 558–567. https://doi.org/10.1175/1520-0469(1973)030<0558:AMFTDO>2.0.CO;2 (1973).
16. Stoll, R., Gibbs, J. A., Salesky, S. T., Anderson, W. & Calaf, M. Large-eddy simulation of the atmospheric boundary layer. *Bound. Layer Meteor.* **177**, 541–581. https://doi.org/10.1007/s10546-020-00556-3 (2020).
17. Marshall, J. & Schott, F. Open-ocean convection: Observations, theory, and models. *Rev. Geophys.* **37**, 1–64. https://doi.org/10.1029/98RG02739 (1999).
18. Julien, K., Legg, S., McWilliams, J. & Werne, J. Penetrative convection in rapidly rotating flows: Preliminary results from numerical simulation. *Dyn. Atmos. Oceans* **24**, 237–249. https://doi.org/10.1016/0377-0265(95)00449-1 (1996).
19. Wang, D. Entrainment laws and a bulk mixed layer model of rotating convection derived from large-eddy simulations. *Geophys. Res. Lett.* **30**, https://doi.org/10.1029/2003GL017869 (2003).
20. Canuto, V. *et al.* Modeling ocean deep convection. *Ocean Modell.* **7**, 75–95. https://doi.org/10.1016/S1463-5003(03)00038-6 (2004).
21. Rossby, C.-G. & Montgomery, R. B. The layer of frictional influence in wind and ocean currents. *Pap. Phys. Oceanogr. Meteorol.* **3**, 1–101. https://doi.org/10.1575/1912/1157 (1935).
22. Gaspar, P. Modeling the seasonal cycle of the upper ocean. *J. Phys. Oceanogr.* **18**, 161–180. https://doi.org/10.1175/1520-0485(1988)018<0161:MTSCOT>2.0.CO;2 (1988).
23. Foltz, G. R., Schmid, C. & Lumpkin, R. Seasonal cycle of the mixed layer heat budget in the northeastern tropical Atlantic ocean. *J. Clim.* **26**, 8169–8188. https://doi.org/10.1175/JCLI-D-13-00037.1 (2013).
24. Sykes, R. & Henn, D. Large-eddy simulation of turbulent sheared convection. *J. Atmos. Sci.* **46**, 1106–1118. https://doi.org/10.1175/1520-0469(1989)046<1106:LESOTS>2.0.CO;2 (1989).
25. Moeng, C. H. & Sullivan, P. P. A comparison of shear- and buoyancy-driven planetary boundary layer flows. *J. Atmos. Sci.* **51**, 999–1022. https://doi.org/10.1175/1520-0469(1994)051<0999:ACOSAB>2.0.CO;2 (1994).
26. Khanna, S. & Brasseur, J. G. Three-dimensional buoyancy-and shear-induced local structure of the atmospheric boundary layer. *J. Atmos. Sci.* **55**, 710–743. https://doi.org/10.1175/1520-0469(1998)055<0710:TDBASI>2.0.CO;2 (1998).
27. Huang, C. J., Qiao, F. & Dai, D. Evaluating cmip5 simulations of mixed layer depth during summer. *J. Geophys. Res.* **119**, 2568–2582. https://doi.org/10.1002/2013JC009535 (2014).
28. Belcher, S. E. *et al.* A global perspective on Langmuir turbulence in the ocean surface boundary layer. *Geophys. Res. Lett.* **39**, https://doi.org/10.1029/2012GL052932 (2012).
29. McWilliams, J. C., Sullivan, P. P. & Moeng, C. H. Langmuir turbulence in the ocean. *J. Fluid Mech.* **334**, 1–30. https://doi.org/10.1017/S0022112096004375 (1997).
30. Grant, A. L. M. & Belcher, S. E. Characteristics of Langmuir turbulence in the ocean mixed layer. *J. Phys. Oceanogr.* **39**, 1871–1887. https://doi.org/10.1175/2009JPO4119.1 (2009).
31. D'Asaro, E. A. Turbulence in the upper-ocean mixed layer. *Annu. Rev. Mar. Sci.* **6**, 101–115. https://doi.org/10.1146/annurev-marine-010213-135138 (2014).
32. Qiao, F. *et al.* Wave-induced mixing in the upper ocean: Distribution and application to a global ocean circulation model. *Geophys. Res. Lett.* **31**, https://doi.org/10.1029/2004GL019824 (2004).
33. Chen, S., Qiao, F., Huang, C. & Song, Z. Effects of the non-breaking surface wave-induced vertical mixing on winter mixed layer depth in subtropical regions. *J. Geophys. Res. Oceans* **123**, 2934–2944. https://doi.org/10.1002/2017JC013038 (2018).

34. Tsujino, H. *et al.* Evaluation of global ocean–sea-ice model simulations based on the experimental protocols of the Ocean Model Intercomparison Project Phase 2 (OMIP-2). *Geosci. Model Dev.* **13**, 3643–3708. https://doi.org/10.5194/gmd-13-3643-2020 (2020).

35. Kato, H. & Phillips, O. On the penetration of a turbulent layer into stratified fluid. *J. Fluid Mech.* **37**, 643–655. https://doi.org/10.1017/S0022112069000784 (1969).

36. Jonker, H. J., van Reeuwijk, M., Sullivan, P. P. & Patton, E. G. On the scaling of shear-driven entrainment: A DNS study. *J. Fluid Mech.* **732**, 150–165. https://doi.org/10.1017/jfm.2013.394 (2013).

37. Ellison, T. Turbulent transport of heat and momentum from an infinite rough plane. *J. Fluid Mech.* **2**, 456–466. https://doi.org/10.1017/S0022112057000269 (1957).

38. Osborn, T. Estimates of the local rate of vertical diffusion from dissipation measurements. *J. Phys. Oceanogr.* **10**, 83–89. https://doi.org/10.1175/1520-0485(1980)010<0083:EOTLRO>2.0.CO;2 (1980).

39. Kirshbaum, D. J. & Straub, D. N. Linear theory of shallow convection in deep, vertically sheared atmospheres. *Q. J. Roy. Meteor. Soc.* **145**, 3129–3147. https://doi.org/10.1002/qj.3609 (2019).

40. Mellor, G. L. One-dimensional, ocean surface layer modeling: a problem and a solution. *J. Phys. Oceanogr.* **31**, 790–809. https://doi.org/10.1175/1520-0485(2001)031<0790:ODOSLM>2.0.CO;2 (2001).

41. Mellor, G. & Blumberg, A. Wave breaking and ocean surface layer thermal response. *J. Phys. Oceanogr.* **34**, 693–698. https://doi.org/10.1175/2517.1 (2004).

42. Nakanishi, M. & Niino, H. An improved mellor–yamada level-3 model with condensation physics: Its design and verification. *Bound. Layer Meteor.* **112**, 1–31, https://doi.org/10.1023/B:BOUN.0000020164.04146.98 (2004).

43. Nakanishi, M. & Niino, H. An improved Mellor–Yamada level-3 model: Its numerical stability and application to a regional prediction of advection fog. *Bound. Layer Meteor.* **119**, 397–407, https://doi.org/10.1007/s10546-005-9030-8 (2006).

44. Nakanishi, M. & Niino, H. Development of an improved turbulence closure model for the atmospheric boundary layer. *J. Meteor. Soc. Jpn.* **87**, 895–912. https://doi.org/10.2151/jmsj.87.895 (2009).

45. Robertson, R. & Hartlipp, P. Surface wind mixing in the regional ocean modeling system (ROMS). *Geosci. Lett.* **4**, 1–11. https://doi.org/10.1186/s40562-017-0090-7 (2017).

46. Yukimoto, S. *et al.* A new global climate model of the meteorological research institute: MRI-CGCM3-model description and basic performance-. *J. Meteor. Soc. Jpn. Ser.* **II**(90), 23–64. https://doi.org/10.2151/jmsj.2012-A02 (2012).

47. Satoh, M. *et al.* The non-hydrostatic icosahedral atmospheric model: Description and development. *Prog. Earth Planet. Sci.* **1**, 1–32. https://doi.org/10.1186/s40645-014-0018-1 (2014).

48. Ushijima, Y. & Yoshikawa, Y. Mixed layer depth and sea surface warming under diurnally cycling surface heat flux in the heating season. *J. Phys. Oceanogr.* **49**, 1769–1787. https://doi.org/10.1175/JPO-D-18-0230.1 (2019).

49. Ushijima, Y. & Yoshikawa, Y. Mixed layer deepening due to wind-induced shear-driven turbulence and scaling of the deepening rate in the stratified ocean. *Ocean Dyn.* **70**, 505–512. https://doi.org/10.1007/s10236-020-01344-w (2020).

50. Deardorff, J. W. Stratocumulus-capped mixed layers derived from a three-dimensional model. *Bound. Layer Meteor.* **18**, 495–527. https://doi.org/10.1007/BF00119502 (1980).

51. Maronga, B. *et al.* The parallelized large-eddy simulation model (PALM) version 4.0 for atmospheric and oceanic flows: model formulation, recent developments, and future perspectives. *Geosci. Model Dev.* **8**, 2515–2551. https://doi.org/10.5194/gmd-8-2515-2015 (2015).

52. Pollard, R. T., Rhines, P. B. & Thompson, R. O. R. Y. The deepening of the wind-mixed layer. *Geophys. Fluid. Dyn.* **4**, 381–404. https://doi.org/10.1080/03091927208236105 (1973).

53. Hosoda, S., Ohira, T., Sato, K. & Suga, T. Improved description of global mixed-layer depth using Argo profiling floats. *J. Oceanogr* **66**, 773–787. https://doi.org/10.1007/s10872-010-0063-3 (2010).

54. Kalnay, E. *et al.* The NCEP/NCAR 40-year reanalysis project. *Bull. Am. Meteor. Soc.* **77**, 437–472. https://doi.org/10.1175/1520-0477(1996)077<0437:TNYRP>2.0.CO;2 (1996).

55. Kara, A. B., Rochford, P. A. & Hurlburt, H. E. Efficient and accurate bulk parameterizations of air-sea fluxes for use in general circulation models. *J. Atmos. Ocean. Technol.* **17**, 1421–1438. https://doi.org/10.1175/1520-0426(2000)017<1421:EAABPO>2.0.CO;2 (2000).

56. Jackett, D. R., McDougall, T. J., Feistel, R., Wright, D. G. & Griffies, S. M. Algorithms for density, potential temperature, conservative temperature, and the freezing temperature of seawater. *J. Atmos. Ocean. Technol.* **23**, 1709–1728. https://doi.org/10.1175/JTECH1946.1 (2006).

Acknowledgements

Author contributions

Y.U. and Y.Y. conceived the experiments, and Y.U. conducted the experiments and analyzed the results. All authors reviewed the manuscript.

Competing interests

The authors declare no competing interests.

Additional information

Supplementary Information The online version contains supplementary material available at https://doi.org/10.1038/s41598-022-14098-w.

Correspondence and requests for materials should be addressed to Y.U.

Reprints and permissions information is available at www.nature.com/reprints.

Publisher's note Springer Nature remains neutral with regard to jurisdictional claims in published maps and institutional affiliations.